



OPEN Shipboard observational evidence of supercooled liquid water clouds in the mid-troposphere over the Southern Ocean

Jun Inoue^{1,2✉}, Kazutoshi Sato^{2,3} & Shingo Shimizu⁴

Clouds are crucial to regulating incoming and outgoing radiation over the ocean. However, there are still large discrepancies between climate models and observations, particularly over the Southern Ocean, which plays a major role in global climate projections. Using shipboard ceilometer and radiometer data, we examine the relationship between the cloud-base temperature and the occurrence frequency of supercooled liquid water (SLW) clouds. Our results indicate that SLW clouds dominate as thin (< 200 m thick) altocumulus in the mid-troposphere with a fraction of about 95%, even under cloud-base temperatures of less than -25°C . These clouds are therefore difficult to reproduce in models with coarse vertical resolution. An underestimation of surface downward longwave radiation was found in atmospheric reanalysis due to the misrepresentation of the mid-tropospheric clouds near 4 km where phase transitions occur. Based on air mass backward trajectory analysis, the clouds associated with the local transport during the non-cyclone period seemed essential for the surface radiation budget.

Keywords Clouds, Southern Ocean, Supercooled liquid water clouds, Climate projection

Solar radiation is a primary energy source that originates outside the Earth. Cloud coverage, the ratio of land to ocean, and land types are essential factors regulating incoming and outgoing solar radiation from the surface albedo viewpoint. The phases of clouds composed of liquid, ice, or both are important in determining the degree of reflection of solar radiation due to the characteristics of backscatter and the concentration of cloud particles¹. This effect is of particular importance in polar regions where solar radiation dominates during the midnight sun. The phase change feedback in polar day is also important in mediating Arctic amplification². During the winter, the longwave radiation from the clouds regulates the surface heat budget³; therefore, the phase of clouds is critical for climate simulation.

In general, ice clouds can form under the presence of ice nucleating particles (INPs), which facilitate ice nucleation under temperature conditions of $> -38^{\circ}\text{C}$. It is thought that INPs are transported to remote regions as dust, activating ice nucleation under relatively low temperatures (e.g., $< -15^{\circ}\text{C}$)⁴, or as bioaerosols, primarily bacteria, from the sea surface under relatively high temperatures (e.g., $> -10^{\circ}\text{C}$)^{5,6}. Efforts of global aerosol transfer models that treat aerosol composition and number concentration are essential to understand the holistic change associated with global warming⁷. Without INPs, supercooled liquid water (SLW) clouds under the freezing point can dominate between 0°C and -38°C depending on the cloud condensation nuclei (CCN) composition and its concentration (e.g. SLW clouds can exist $< -25^{\circ}\text{C}$)⁸. For example, climate models underestimated CCN number concentrations by roughly 50%⁹. The low bias in SLW and the associated radiation biases over the Southern Ocean (SO) has been well-established for over a decade^{10,11}. Attempts have been made in climate models with clouds over the SO to reduce the overestimation of ice clouds. The relationship between the fraction of SLW clouds and the temperature given the presence of clouds is usually investigated using satellite products as a reference¹². Temperatures between -30°C and -20°C constitute a transitional zone from the

¹Arctic Environment Research Center, National Institute of Polar Research, 10-3 Midori-cho, 190-8518 Tachikawa, Tokyo, Japan. ²Polar Science Program, The Graduate University for Advanced Studies, SOKENDAI, 10-3 Midori-cho, 190-8518 Tachikawa, Tokyo, Japan. ³International Polar and Earth Environmental Research Center, National Institute of Polar Research, 10-3 Midori-cho, 190-8518 Tachikawa, Tokyo, Japan. ⁴Department of Extreme Weather Disaster Research, National Research Institute for Earth Science and Disaster Resilience, 3-1 Tennodai, Ibaraki, 305-0006 Tsukuba, Tokyo, Japan. ✉email: inoue.jun@nipr.ac.jp

liquid to ice phase. Most climate models in the Fifth Assessment Report of the Intergovernmental Panel on Climate Change overestimate the ratio of ice cloud occurrence compared with satellite products¹¹. However, the models in the Sixth Assessment Report have improved this relationship in recent decades¹³.

To maintain SLW clouds, the increase of vertical resolution¹⁴, and a new microphysical parameterization which allows SLW cloud formation near the cloud top even in coarse vertical resolution¹⁵ have been proposed. The NCAR Community Earth System Model version 2¹⁶ succeeded in representing the SO clouds via adjustments to the ice nucleation and cloud microphysics schemes that permit additional SLW clouds; however, improvements in the ice nucleation processes are still required because the quantity of ice clouds became too small compared with aircraft observations. Sensitivity tests focusing on marine and mineral dust INPs have concluded that model biases in the simulated sea salt and high variability in the mineral dust aerosols contribute to the uncertainty and variability in the model-predicted INP populations¹⁷. Satellite observation showed that SLW clouds dominate at the mid-troposphere with a thin structure¹⁸. Because their vertical structure might make it challenging to represent climate models, the kinematic process, such as wind shear, would be a source of shallow convection¹⁹.

The representation of the radiation balance at the cloud top has been discussed in the climate model community²⁰ because satellite datasets are available for validation at a global scale for each season. Surface radiation observations, including ground-based remote sensing for clouds and precipitation, are also essential to understand the impact of the cloud vertical structure on the surface heat budget²¹. The underestimation of SLW clouds and cloud liquid water paths in a cyclone caused a large downward shortwave (DSW) radiation error in the climate models over the SO²². In the case of ERA5 reanalysis²³, the mean bias of surface DSW radiation exhibited 54 W m^{-2} ²⁴. Downward longwave (DLW) radiation is also a fundamental component when discussing the representation of clouds, in particular their phases, ceilings, and temperatures. In the Arctic Ocean, shipboard measurements based on radiosondes, ceilometers, and C-band Doppler radar were used as validation data for a regional climate model intercomparison project²⁵, contributing to the identification of characteristics of model parameterizations for cloud microphysics, boundary layer processes, and radiation schemes. Aircraft observations would be useful to capture the spatial scales of cloud systems over polar oceans^{26,27}; however, this type of study provides only a snapshot, making applications to modeling difficult. Shipborne observations, conversely, can capture extended time ranges of more than a month, enabling the capture of several atmospheric events as well as normal conditions.

This study used cruise data (Fig. 1a) obtained by a shipboard lidar ceilometer and microwave radiometer to focus on the relationship between the temperature at which clouds exist and their phase. The ceilometer can monitor the cloud phase at the cloud base. At the same time, the microwave radiometer can obtain the air temperature at the cloud base, enabling an estimation of the relationship between the cloud-base temperature and the frequency of SLW cloud occurrence.

Results

Characteristics of observed clouds

Figure 1b shows a scatter plot of the cloud-base temperature and its height, as detected by the microwave radiometer and lidar ceilometer, distinguishing each cloud phase (red: liquid water clouds and blue: ice clouds) during the four-month cruise over the SO and near the Antarctic coast. While the ceilometer cannot detect the inner state of the clouds, it provides high-temporal-resolution data (every minute), yielding a large dataset of cloud phase observations at the cloud base. Although the estimation of cloud-base temperature had a relatively larger error as the temperature decreased below $-15 \text{ }^\circ\text{C}$, as shown in Supplementary Fig. 1, the number of samples was limited, in particular, below $-30 \text{ }^\circ\text{C}$. SLW clouds were frequently observed at a temperature of $> -25 \text{ }^\circ\text{C}$ (more than 95% of samples; gray bars in Fig. 1c). Although ice nucleation at higher temperature is possible if a certain amount of INPs exist, the more than 98% fraction of SLW clouds under the $> -25 \text{ }^\circ\text{C}$ condition suggests that the effect of INPs in the lower troposphere is minimal. The exception (a few percent of samples) would be mid-level ice clouds formed by the long-range transport of INPs originating from the sea surface at mid-latitudes²⁸, likely associated with an atmospheric river event.

The red line in Fig. 1c shows the SLW cloud occurrence frequency at each temperature range, binned every 5 K. This frequency is not comparable with the mass fraction of SLW in the mixed-phase clouds, including the precipitating SLW clouds, because the ceilometer detects the cloud-base information. The frequency is nearly 95% under the temperature condition of $> -25 \text{ }^\circ\text{C}$ with a large number of samples, while it is nearly zero in the case of $< -40 \text{ }^\circ\text{C}$ with a minimal number of observed samples. The transitional temperature zone is at -35 – $-25 \text{ }^\circ\text{C}$ where cloud-base heights were observed between 3 km and 6.5 km, i.e., in the mid-troposphere (Fig. 1b).

The cloud-base height frequency distribution relative to the entire observation period during the cruise (red bars in Fig. 2) indicates that a lower ceiling below 1.5 km dominated, as shown in the literature²⁹. Compared with boreal summertime Arctic clouds, where the lowermost clouds ($< 0.5 \text{ km}$) dominate, with a more than 60% occurrence as stratus clouds over the ice-free ocean³⁰, the difference in the SO is that the frequency of the lowermost clouds ($< 0.5 \text{ km}$) was not significant (15%), suggesting the presence of a wide variety of cloud-base heights, partly related to frequent synoptic disturbances. Note that mid-tropospheric clouds (3–5 km) were observed to comprise more than 15%. The same analysis was made for the ERA5 hourly atmospheric reanalysis²³ along the cruise track (gray bars in Fig. 2); however, the representation of lower tropospheric clouds ($< 1 \text{ km}$) was nearly doubly overestimated, while mid-tropospheric clouds ($> 3 \text{ km}$) were underestimated by half compared with observations. The ERA5 represented clear-sky conditions much worse than the other reanalysis³¹, as it showed a much higher cloud fraction under satellite-observed clear-sky conditions, which supports the overestimation of lower tropospheric clouds in this study. The underestimation of mid-tropospheric clouds might be caused by several issues, as discussed later (e.g., an issue of wind shear).

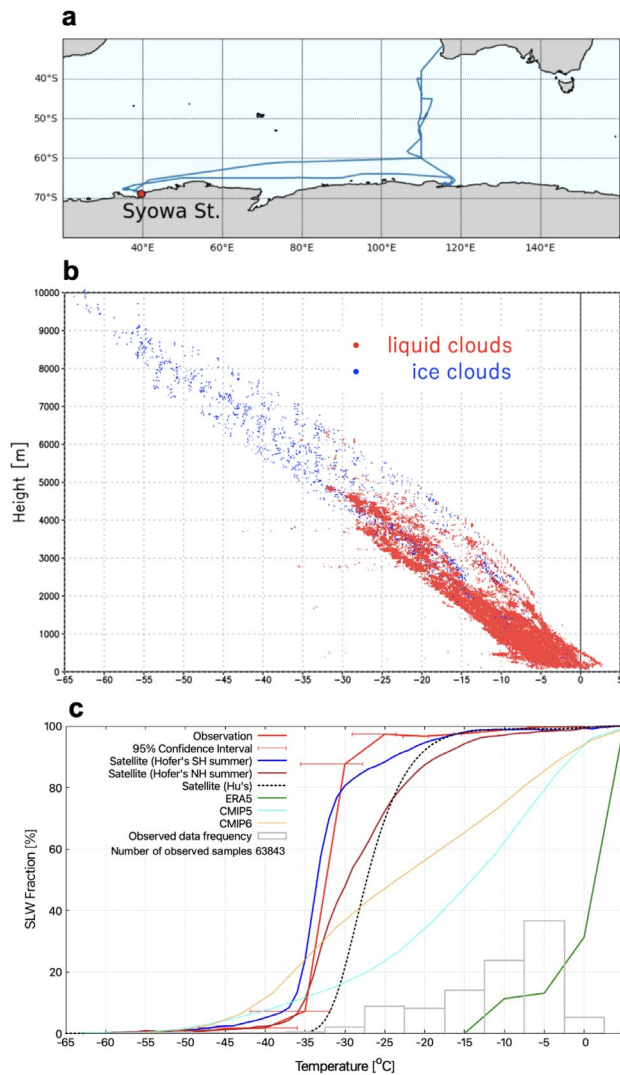


Fig. 1. Cruise track, cloud-base temperature and phase, and liquid water cloud fraction. **(a)** Cruise track in which the data were collected (the red mark indicates the location of Syowa Station where operational radiosonde observations were made). **(b)** Cloud-base temperature derived from the microwave radiometer and lidar ceilometer. Red and blue marks indicate spherical particles (supercooled liquid droplets) and non-spherical particles (ice crystals), respectively, based on the linear depolarization ratio from the lidar ceilometer. The data period is from December 2, 2022, to March 16, 2023. **(c)** Observed supercooled liquid water (SLW) cloud fraction (red), with reference lines based on satellite and model data (the cloud top from CALIOP south of 30° S during December–February⁴¹ (blue); the same as the blue line but north of 30° N during July–August (brown); annual global CALIOP cloud top products for mid-layer clouds¹² (black), hourly cloud-base data from ERA5 reanalysis during the observations²³ (green); and the ratio of liquid water path to total water path from global CMIP5 (cyan) and CMIP6 (orange) outputs¹³), and the observed data frequency (gray) as a function of temperature. The error bars indicated the temperature estimation with a 95% confidence level based on the regression line shown in Supplementary Fig. 1.

To focus on the mid-tropospheric clouds, an example of a time–height cross section of the attenuated backscatter coefficient (*ABS*) when typical mid-tropospheric SLW clouds persisted near Syowa Station is shown in Fig. 3a. The cloud-base height at close to 3 km was continuously observed, with some attenuation caused by lower clouds. These clouds were usually independent of the lower boundary layer clouds except in cases of synoptic storms²⁸. The chance of observations of these clouds as the first layer by the ceilometer was relatively high when lower boundary layer clouds were absent. Based on the linear depolarization ratio (*LDR*), these clouds were SLW clouds (spherical *LDR* signals) with light snowfall (non-spherical *LDR* signals; brownish shadings in Fig. 3b). The visual state of these clouds on this day can be confirmed via images taken by a forward-looking camera on the ship (Fig. 4b). The primary cloud type was likely altocumulus, which was based on visual appearance. The relative humidity with respect to liquid saturation obtained by radiosondes at 23:30 UTC on December 25, 2022 at Syowa Station (Fig. 3d) revealed that the humid layer where this mid-tropospheric cloud layer existed was generally geometrically thin (< 200 m thick); therefore, the vertical resolution of the

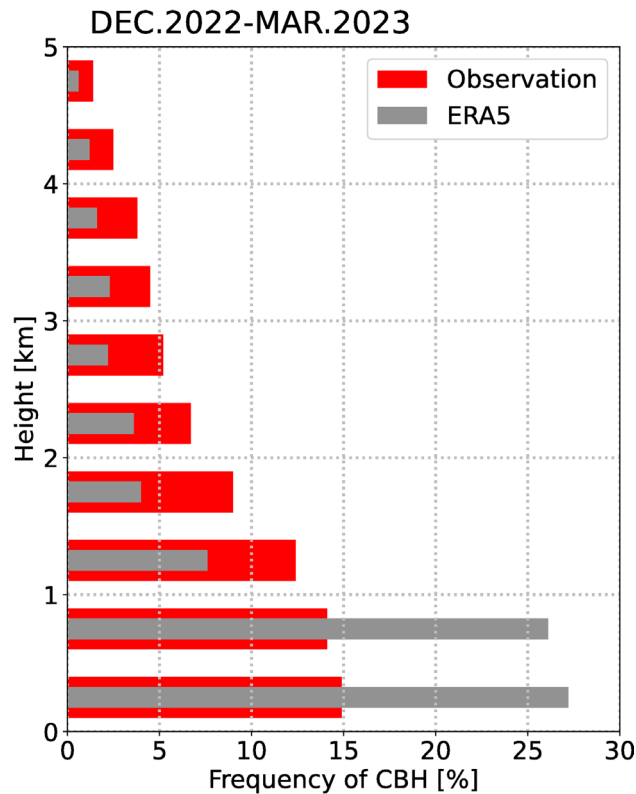


Fig. 2. The cloud-base height frequency distribution relative to the entire observation period. The data were obtained by the lidar ceilometer (red bars) and ERA5 (gray bars) during an overcast period of the cruise.

models sometimes hindered their reproduction, as shown in Fig. 2. In addition, a wind directional shear from northeasterly below 3.2 km to northwesterly above the cloud top was found (Fig. 3e), suggesting that other air mass sources from remote regions riding up on the lower boundary layer presumably generated undulatus clouds. These geometrically thin clouds were frequently observed during the cruise, as shown in Fig. 4, which agrees with the non-negligible frequency of the cloud-base height above 3 km, as shown in Fig. 2.

Impact of cloud phase on surface radiation

How do altocumulus clouds influence the surface radiation environment? The failure to represent mid-tropospheric SLW clouds in ERA5 causes radiation biases at sea and sea-ice surfaces because the altitude near 4 km is the transitional temperature zone for the cloud base for liquid or ice phases (Fig. 1b). Figure 5 shows the relative frequency of the DLW and DSW radiations observed on the ship and estimated in ERA5. Overall, the DLW radiation distribution in ERA5 was shifted 10–20 W m^{-2} lower than the observation (Fig. 5a). The primary observed peak near 295 W m^{-2} with an approximate 20% frequency, most likely for the case of lower tropospheric cloud conditions, was larger than that in ERA5 (285 W m^{-2}) with an approximate 10% frequency. The value of the observed peak frequency was nearly doubled; this is inconsistent with the cloud-base height frequency (Fig. 2) if the dominant cloud phase in ERA5 is also SLW clouds. This discrepancy likely arises from the cloud phase error in ERA5. Because the emissivity of ice clouds is approximately 0.90 at most, based on satellite observations³², which is smaller than the typical liquid water emissivity (> 0.97)³³, the replacement of the cloud phase from SLW to ice clouds would lead to an underestimation of the most frequent value of DLW. In most of the lower part from the peak (265–285 W m^{-2}), considered to be overcast conditions with a lower temperature cloud bottom (i.e., mid-tropospheric clouds), the observed frequency was greater than those in ERA5.

The secondary peak at 225 W m^{-2} was also shifted to 205 W m^{-2} in ERA5. In this secondary peak, which is likely related to clear sky or low cloud cover conditions, ERA5 seemed to have less cloud cover than observed. Note that the observed DLW radiation during the occurrence of altocumulus clouds ranged between 205 W m^{-2} and 275 W m^{-2} (Fig. 4); therefore, this secondary peak would still include the cases of altocumulus clouds under various cloud covers and cloud-base heights. Based on the comparison of the DSW, the value between 325 W m^{-2} and 775 W m^{-2} in ERA5 overestimated approximately 1% of frequencies (Fig. 5b), suggesting the overestimation of ice clouds instead of SLW clouds (less reflection of shortwave radiation at the cloud top). The averaged DSW radiation in ERA5 was overestimated by 33 W m^{-2} compared with the observations during the cruise (a net downward radiation bias of 12 W m^{-2} is still significant). Therefore, the misrepresentation of ice clouds in atmospheric reanalyses strongly influences the evaluation of the surface radiation.

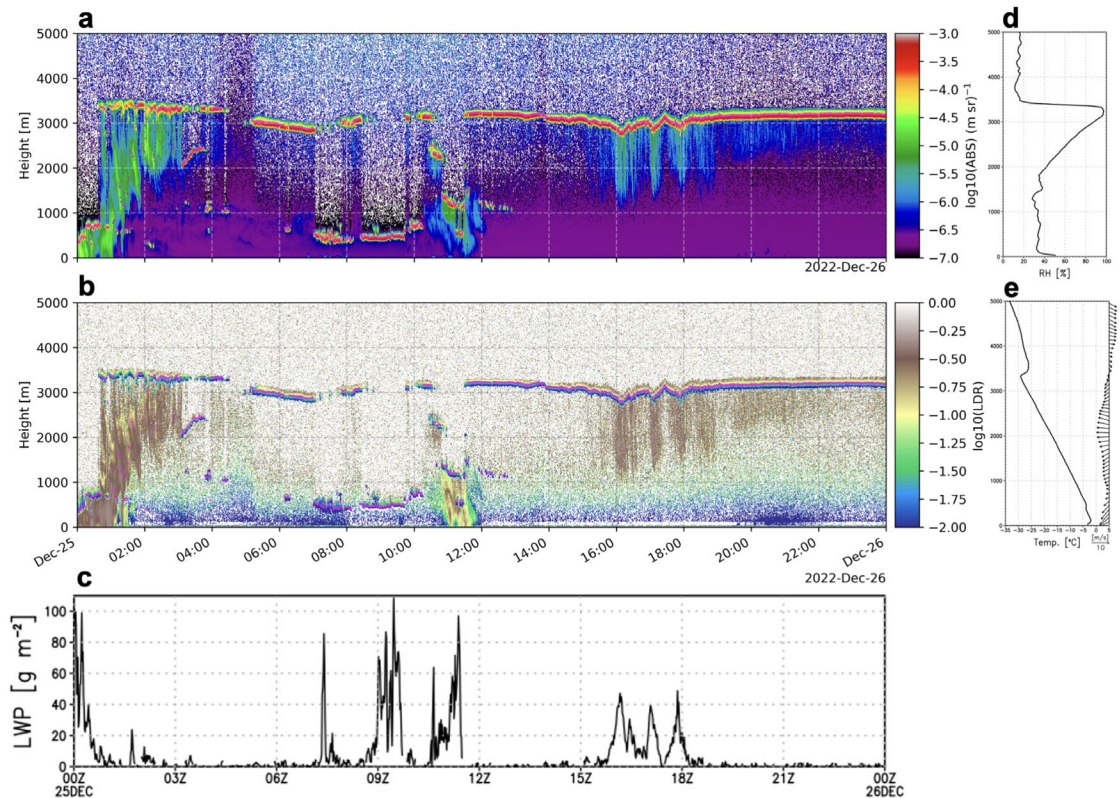


Fig. 3. Time-height cross-section of the lidar ceilometer data and radiosonde profile. **(a)** Absolute backscatter coefficient (*ABS*), and **(b)** linear depolarization ratio (*LDR*) obtained by the ceilometer. A magenta line for each panel indicates the cloud bottom height detected by the ceilometer. The higher value of *ABS* indicates the stronger reflection of the signal (e.g., clouds and precipitation). Lower (≤ -1.17), middle ($-1.17 < \log_{10}(LDR) \leq -0.35$), and higher (> -0.35) $\log_{10}LDR$ indicate the cloud droplets, ice crystals, and snow, respectively. **(c)** liquid water path observed by the microwave radiometer, **(d)** relative humidity, and **(e)** air temperature with horizontal wind vectors from a radiosonde at Syowa station at 23:30UTC.

Altostratus formation and their impact on surface radiation

Altostratus clouds often consist of a thin SLW layer (a few hundred meters) with a sub-cloud layer containing several narrow virga fall streaks³⁴. Figure 3b clearly shows that the altostratus cloud at 3.1 km had a virga layer down to 1 km at 16:00 UTC on December 25. When the backscatter of the virga strengthened several times between 16:00 and 19:00 UTC (Fig. 3a), the base height of the SLW cloud coincidentally decreased. Based on the microwave radiometer measurement, the liquid water path increased from near zero (usually undetectable for the thin SLW layer) to 40 g m^{-2} during this period. SLW-generating cells would be intensified by radiative cooling at the cloud top and by turbulent mixing in the layer, deepening sub-cloud virga³⁵. This feature was also observed in other field observations over the SO using ship-based cloud radar and lidar³⁶. After this period, the depth of the virga gradually thinned to 2.5 km late in the day. According to an analysis of the satellite product¹⁸, the probability frequency of mid-tropospheric liquid clouds at 2–5 km over the SO would have originated from thin SLW clouds whose average thickness was 330 m.

The most lasting period of the SLW in the mid-troposphere was from 23 December to 27 December 2022. A time-height cross-section of cloud-base height with horizontal winds and their vertical shear based on radiosonde data at Syowa station, which was close to the ship (Fig. 6a), showed there could be a relatively strong vertical wind speed shear above the cloud base ($> 10 \text{ ms}^{-1} \text{ km}^{-1}$). The lifetime of SLW clouds was typically half a day to a few days, depending on how long such a wind condition was sustained, although the coarse time resolution of radiosondes limits further analysis.

The strong wind shear is a favorable environment for generating clouds induced by Kelvin-Helmholtz Instability (KHI). Richardson number (*Ri*), the ratio of static stability and the wind shear squared are usually used to assess the environment for KHI ($Ri < 0.25$). However, this situation is rarely observed by radiosondes because the layers with $Ri < 0.25$ should quickly become turbulent and raise *Ri* to more stable values³⁷. The statistical analysis of the Mesosphere-Stratosphere-Troposphere/Incoherent Scatter radar at the Syowa station showed that the KHI frequently occurred between 3–6 km, and background median wind shear and *Ri* was $12.3 \text{ m s}^{-1} \text{ km}^{-1}$ and 1.17, respectively¹⁹. Therefore, a representation of high wind shear, even in relatively high *Ri* in climate models, is one of the essential physical conditions for the SLW cloud formation.

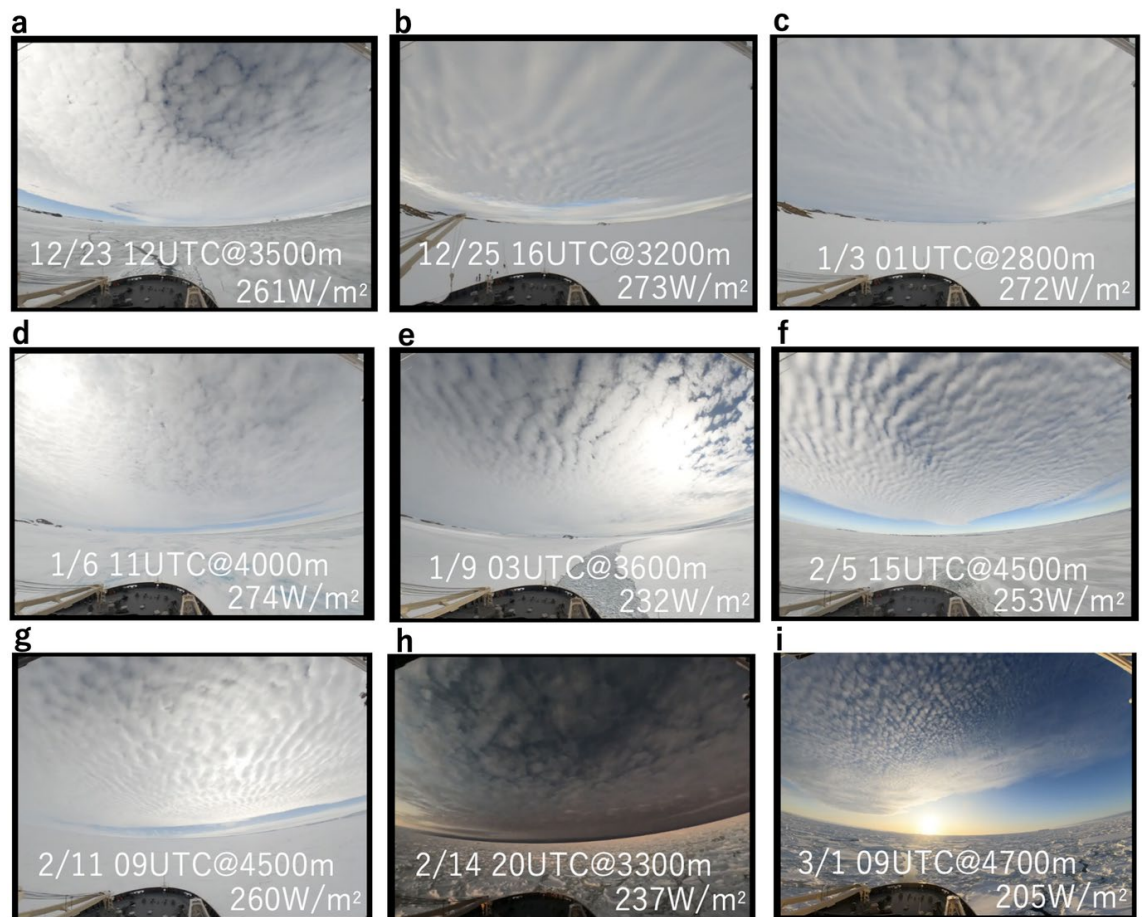


Fig. 4. Altocumulus clouds over the Southern Ocean and Antarctic coast. Photos were taken by a forward-looking camera each day. The height and radiation indicated in each photo are the approximate cloud-base height according to the ceilometer and the downward longwave radiation, respectively.

The radiative transfer model *Streamer*^{38,39} was used to estimate the radiative effect of the SLW clouds as a case study of 23:30 UTC on 25 December. Using the radiosonde data at Syowa station and defining the cloud layer where relative humidity > 95%, the DLW and DSW radiations were estimated in the two cases of clouds: a control run is the realistic case of the SLW clouds and the other is a sensitivity run of ice clouds. The surface DLW radiation in the control case ($258 W m^{-2}$) was closely matched with the observed one ($251 W m^{-2}$; blue square in Fig. 6b), while the radiation in the case of ice cloud ($218 W m^{-2}$) was significantly underestimated compared with observation. The difference in the longwave cloud radiative effect is $40 W m^{-2}$, suggesting the cloud phase error causes critical influences on the frequency of the radiation field as in Fig. 5a. This error is sometimes compensated by the shortwave cloud radiative effect when the DSW radiation is small, such as in this case.

The impact of cloud phase error on DSW radiation was also assessed using the same setting of the radiative transfer model but with a change in the local time ahead of 12 h, assuming a high solar zenith angle case, as shown in Fig. 6c. The DSW was overestimated by $154 W m^{-2}$ when the SLW clouds were replaced as ice clouds. This discrepancy influences the frequency distribution of DSW radiation in Fig. 5b and the surface radiation budget. Total cloud radiative effect for SLW and ice clouds were $-68 W m^{-2}$ and $-21 W m^{-2}$, suggesting the cloud phase error causes additional surface heating $47 W m^{-2}$.

Thermodynamic environments for altocumulus

SLW clouds at temperatures lower than $-30^{\circ}C$ can occur if the ice crystal concentrations and sizes are sufficiently small with a weak updraft⁴⁰. Recent satellite analyses, distinguishing between cloud-top and interior phases in mixed-phase clouds, reveal that mixed-phase clouds are more liquid globally at the cloud top, particularly over the SO, without seasonal variability⁴¹. The fraction of SLW clouds south of $30^{\circ}S$ as a function of temperature under the $> -30^{\circ}C$ condition during austral summer was more than 80% (blue line in Fig. 1c), which is similar to our observation (red line in Fig. 1c) (note that these data comparisons were not made explicitly due to difficulty in fitting the collocation and co-incident). The SLW fraction in boreal summer (brown line in Fig. 1c) is 10%–20% smaller than that in austral summer, probably because the remote transport of INPs above the mid-troposphere originating from terrestrial regions could contribute to additional ice cloud formation. Classifying low-, mid-, and high-level clouds during winter and summer over the SO²⁸, the SLW

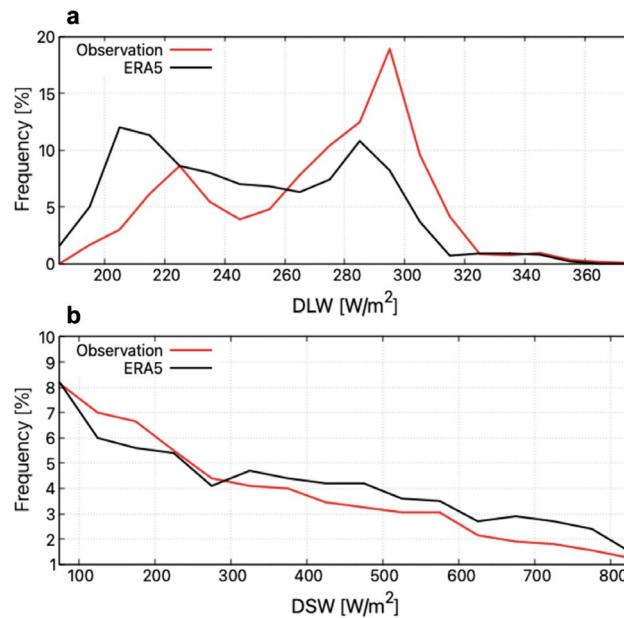


Fig. 5. Frequency distribution of the downward radiation. **(a)** Downward longwave radiation, and **(b)** downward shortwave radiation during the cruise. The red lines indicate the observation averaged for both the port and starboard sides on the ship. The black lines are based on the ERA5 reanalysis.

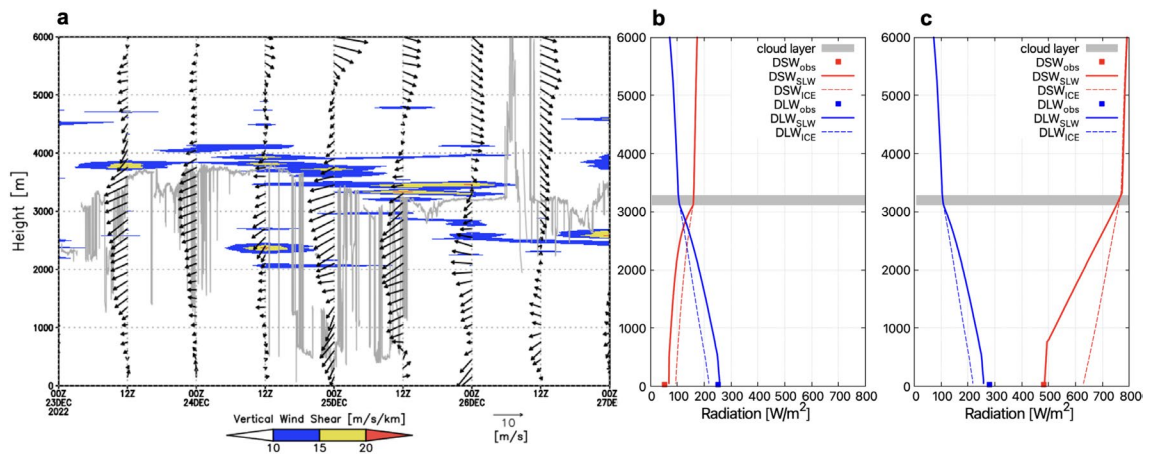


Fig. 6. Relationship among wind shear, radiation, and clouds. **(a)** Time-height cross-section of vertical wind shear defined as $\sqrt{(\delta u/\delta z)^2 + (\delta v/\delta z)^2}$ by the radiosonde data at Syowa station between 2000 and 5000 m (shading). Vectors and gray lines indicate horizontal winds by radiosondes and cloud-base height by the ceilometer. **(b)** Downward longwave radiation (blue) and downward shortwave radiation (red) at 23:30 UTC on 25 December 2022. Solid and dotted lines are indicated in the cases of SLW clouds with a $20\mu\text{m}$ effective radius and ice clouds with a $100\mu\text{m}$ effective radius. The integrated cloud water path was set to 15 g m^{-2} for each case. Squares indicate the surface observation at the same time. **(c)** Same as **(b)**, but at 11:30 UTC on 25 December assuming a high solar zenith angle. Note that meteorological profiles used for calculation are the same as **(b)**.

cloud fraction was more than 60% both in summer for mid-level clouds and winter for low-level clouds even in the temperature $< -30\text{ }^\circ\text{C}$. Although the observation data in this study was very limited and the method to estimate the SLW cloud fraction was different from the satellites and climate models, the feature that the SLW cloud dominated under lower temperatures partly reflects the ordinal situation during summer over the SO. If precipitating snow is considered a part of the clouds, the altocumulus clouds observed by the ceilometer in this study can be classified as mixed-phased clouds, suggesting that the cloud system is not homogeneously mixed in the vertical direction. In other words, the ceilometer measures the upper part of the mixed-phased clouds under these conditions because this study distinguished between the SLW clouds, ice crystals, and snow strictly when using the ceilometer, as described in the Methods.

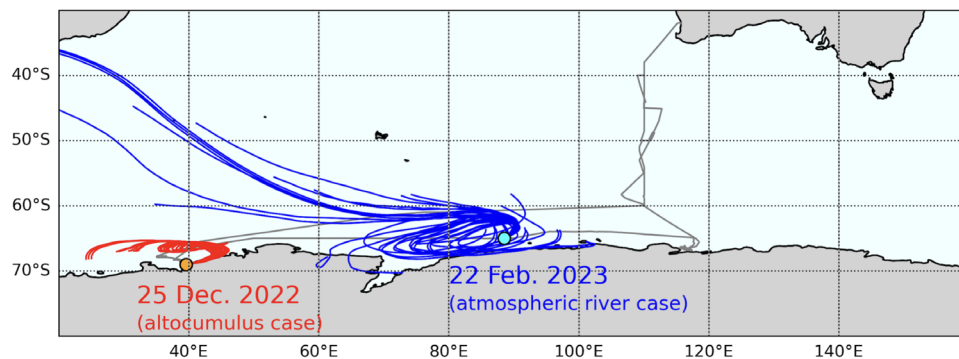


Fig. 7. Backward trajectory map on the SLW cloud case and atmospheric river case. Three-day 27-ensemble backward trajectories starting from 23:00 UTC 25 December 2022 (red lines) and from 13:00 UTC 22 February 2023 (blue lines). The initial height is 3000 m. The former case corresponds to the altocumulus case as SLW clouds. The latter is an ice cloud case associated with an atmospheric river event²⁸. Color dots indicate the ship position for each case. The gray line denotes the ship track.

Discussion

The representation of mid-tropospheric clouds in the Coupled Model Intercomparison Project Phase 6 (CMIP6) was improved compared with that in CMIP5 (Fig. 1c); however, there is still a ~5% negative cloud fraction bias over the SO (55–70° S) compared with satellite-based products⁴². The height and temperature for the modeled mid-tropospheric clouds were 2–5 km and –15 to –25 °C, respectively. These height and temperature ranges correspond to those frequently observed in this study as SLW clouds (Fig. 1b). Several methods have been applied to climate models to reduce ice clouds and increase SLW clouds. In climate models, the vertical resolution in the middle troposphere where altocumulus clouds exist is usually coarser than 500 m. The relative importance of different physical processes needed to maintain SLW clouds was proposed as a reason to increase the vertical resolution. For example, simulations with 500-m resolution had only 5% of the SLW clouds modeled in 50-m simulations because of the decrease in the ice growth rate via vapor deposition in the simulation with a fine resolution, the so-called Wegener–Bergeron–Findeisen mechanism¹⁴. Because simulations at coarser vertical resolutions using a grid box lead to biased mixed-phase microphysical process rates and affect the diagnosis of thin SLW clouds, the SLW layer quickly became glaciated and the altocumulus cloud lifetime was underestimated. A new parameterization for the vertical gradients of the ice–water mixing ratio and temperature in the microphysics calculations allowed SLW clouds to form near the cloud top even at coarse vertical resolution with appropriate radiative cooling at the cloud top and turbulent mixing in the cloud layer¹⁵. This scheme maintained a balance between the depositional ice growth below the SLW clouds and the reformation of SLW clouds via adiabatic condensation with compensating vertical velocity. However, this scheme was based on observations at mid-latitudes, which raises a question concerning its application to the SO. Moreover, the process for increasing INP formation by the secondary ice production with multiple updrafts is also present⁴³, which needs to be considered for cloud microphysics and vertical velocity.

A more straightforward approach is the parameterization of INPs over the SO based on INP observations. The fact that SLW clouds dominated rather than ice clouds suggests that the concentration of INPs was smaller than expected. Using sophisticated cloud and aerosol observations over the SO²⁷, the size distribution of INPs was obtained⁴⁴; this distribution is over two orders of magnitude smaller than the function usually used in climate modeling. Adapting the ice nucleation parameterization reproduced the SLW layers effectively even when the vertical resolution at the layer was set to be coarse by default⁴⁵. This means that customizing the INP size distribution for the SO is crucial for regional climate modeling. However, surface-based aerosol sampling during the limited season hampers our understanding of the mid-tropospheric environment⁴⁶. Clouds, accompanied by synoptic disturbances and atmospheric rivers, are presumably influenced by long-range-transported aerosols, which differ from the background INP size distribution over the SO. For example, one observation showed a discontinuous change in the vertical cloud phase in the mid-troposphere when the air mass originated from the tropical Indian sea surface along the blue tracks in Fig. 7²⁸. Regarding the degree of local emission of INPs at high latitudes, Arctic dust emitted from ice- and vegetation-free areas has a remarkably high ice-nucleating ability⁴⁷ and would influence the cloud radiative effect at the top of the atmosphere and the surface downwelling radiative flux in the Arctic⁴⁸. Seaspray containing organic matter also has the potential as a source of INPs and the formation of ice clouds in the lower boundary layer⁴⁹. Although these processes would also be plausible in SO and Antarctic coastal regions, they are not responsible for the presence of SLW in the mid-troposphere.

A serious issue is that ERA5, an essential dataset for illuminating the current climate status over the last several decades, also underestimates persistent altocumulus clouds (Fig. 2). ERA5 sometimes performs well in the Arctic from the viewpoint of clouds and surface radiation compared with state-of-the-art regional climate models²⁵. The microphysics scheme in ERA5⁵⁰ treats SLW and ice clouds as prognostic variables, which differs from the diagnostic temperature-dependent liquid/ice phase split in the previous scheme (the threshold was –23 °C), ideally leading to a greater chance of SLW clouds between 0 °C and –38 °C; however, the presence of SLW clouds below –20 °C in ERA5 was barely represented in the Arctic summer condition²⁵. As

in the literature⁵⁰, the bimodal distribution of the DLW radiation in the scheme used in ERA5 was not as well separated as in the observed distribution. This tendency was also found in this study (Fig. 5) partly because the incorrect cloud phase, fraction, and base height are potential sources of errors, in particular under the lower temperature conditions of the cloud base (e.g., $-20\text{ }^{\circ}\text{C}$). ERA5 provides the cloud-base height, enabling an analysis of the occurrence frequency of SLW clouds versus ice clouds in the same manner (Fig. 1c), although the time resolution is 1 h instead of 1 min. Because ERA5 permits mixed-phase clouds in a grid, this analysis categorized such clouds as SLW clouds to confirm how the model overestimated just the ice clouds. As expected, the frequency of the sum of SLW and mixed-phased clouds was poorly reproduced (green line in Fig. 1c) compared with observations (even if the observed data was extracted to hourly data for the direct comparison of ERA5, the observed characteristics of data frequency and SLW cloud fraction as a function of temperature were close to the full sample of the observation data). The frequency was approximately zero under the condition of $< -15\text{ }^{\circ}\text{C}$ (i.e., overestimation of ice clouds). The ice cloud-base height was mainly 1.5–2 km (Fig. 1b), consistent with underestimation of the DLW radiation (Fig. 5a). In general, the depositional ice growth rate heavily depends on the number concentration of INPs; choosing the function of the INP concentration as a function of the temperature is critical. The INP function used in ERA5 was based on field observations at a western US mountain range⁵¹. The alternative formulation, a more-than-one-order smaller INP concentration than the former⁵², provided a better fit to the INPs based on Arctic observations in the fall. A comparison between these two formulations indicates that the Arctic INP formulation suppressed the deposition rate by approximately a factor of 5 and increased the amount of SLW with long-lasting and deeper Arctic boundary layer cloud systems⁵⁰; however, ERA5 does not apply this Arctic INP formulation to maintain the global tropospheric consistency across different meteorological regimes. Even in the Arctic INP formulation, the concentration under $> -30\text{ }^{\circ}\text{C}$ is too high compared with the Antarctic INP formulation⁴⁵, suggesting the need for regional INP formulations for global modeling. Comprehensive field observations^{9,44} also reveal small INP sources over the SO, suggesting that the cloud-phase negative feedback would be weak⁵³. The same situation is also expected in the Arctic when the INP supply is small².

The four-month observation in this study contained various clouds as seasonal representations, including very thin clouds. In contrast, airborne observations aiming to capture specific events sometimes would not fit the seasonal feature, for example, indicating less SLW cloud frequency ($< 5\%$) at $-20\text{ }^{\circ}\text{C}$ ⁵⁴, which might be related to long-range air mass transport or local secondary ice production. The seasonal march from the austral summer to autumn would also reduce the SLW cloud frequency (e.g., around 50% at $-10\text{ }^{\circ}\text{C}$ in the austral autumn⁵⁵). The vertical distribution of clouds also heavily depends on the moisture transport. The three-day backward trajectory analysis using the HYSPLIT model⁵⁶ showed the air mass at 3000 m on 25 December 2022 stagnated near the Antarctic coastal region (red lines in Fig. 7). On the other hand, the air mass of the atmospheric river event on 22 February 2023, which contained ice clouds at 3000 m²⁸, crossed the SO, suggesting the long-range moisture transport from the mid-latitudes (blue lines in Fig. 7). In summary, this limited data analysis implies that the vertical distributions of moisture and INPs over the SO might be mainly determined by two modes: a local transport mode during the non-cyclone period, and a long-range transport mode associated with synoptic atmospheric disturbances. The former modes are critical for evaluating the surface radiation budget led by SLW clouds, while the latter is essential for understanding the ice sheet mass balance through precipitation.

Methods

Observations

A lidar ceilometer (CL61, Vaisala Inc. Ltd., Finland) and a microwave radiometer (HATPRO-G4, Radiometer Physics GmbH, Germany) were installed on the research vessel (RV) *Shirase*, which cruised along the SO Antarctic coasts from December 2022 to March 2023 (Fig. 1a). A lidar ceilometer can provide cloud-base heights of up to five layers, the ABS, and the LDR. The cloud structure can be detected if the clouds are optically thin. The temporal and vertical resolutions were 1 min and 4.8 m, respectively (measurement accuracy: $\pm 5\text{ m}$). The maximum detectable altitude was 15.4 km; however, most cloud bases were detected below 10 km on this cruise. The vertical structure of the SLW clouds detected by the CL61 ceilometer agreed well with those from cloud particle sensor sondes (CPS sonde, Meisei Inc. Ltd., Japan), which also detected the phase of the cloud particles and their number and size^{6,57}. The thresholds for identifying the sphericity of the particles are summarized in the CL61 user guide⁵⁸. However, snow particles should be excluded from analyses to minimize errors in the cloud-base temperature. The LDR for snow (0.2–0.4) and ice crystals (0.32<) overlap, which makes it challenging to analyze the cloud-base temperature in this study. In situ cloud observations by drones from the RV *Shirase* revealed that a LDR value of 0.45 is the threshold between the snow particles and ice crystals⁵⁹. In this study, LDR larger than 0.45 and ABS smaller than $10^{-4}\text{ m}^{-1}\text{ sr}^{-1}$ were used to evaluate the ice cloud-base height.

The HATPRO-G4 radiometer continuously obtained the vertical structure of the air temperature (7 channels: 51–58 GHz) and moisture (7 channels: 22.24–31.4 GHz from the surface to 10 km (vertical resolutions are finer at lower altitudes from 10 m to 200 m). To retrieve these parameters, the manufacturer customized a neural network for Antarctica and the SO based primarily on radiosondes of Antarctic coastal regions. Temperature accuracy is between 0.25–1.00 K depending on range height. In this study, the product was further corrected using the results of radiosonde observations at Syowa Station (69.01° S , 39.59° E) (Fig. 1a), as shown in Supplementary Fig. 1 and Supplementary Note. The missing data mainly arose from mechanical issues (e.g., the abnormal elevation angle of the antenna) (Supplementary Fig. 2). Liquid water path (LWP) can also be estimated using two channels (23.8 and 31.4 GHz)⁶⁰. The accuracy of LWP estimation is 20 g m^{-2} .

Radiation measurements were made on the upper deck of the ship on both the starboard and port sides. MS-40C (EKO, Inc. Ltd., Japan) shortwave radiometers were used (temperature dependence: $< \pm 3\%$). The infrared radiometer on the starboard side was an IR02 (Hukseflux, Inc. Ltd., The Netherlands; temperature dependence: $< \pm 3\%$), while that on the port side was an MS-21 (EKO, Inc. Ltd., Japan; temperature dependence: $< \pm 1\%$).

The data were the instantaneous data per minute. The instruments were installed on a 1.5-m-long pole extended beyond the deck to minimize several ship effects (e.g., the shadows of the masts and infrared radiation from the ship body). Automated weather systems were also installed near the radiometers on both sides (starboard side: WXT536, Vaisala, Inc. Ltd.; port side: WS500, Lufft, Inc. Ltd.). A forward-looking camera (Hero9, Gopro Inc. Ltd., USA) was installed in front of the upper deck to monitor the visual state of the clouds. The measuring interval was 5 min. All instruments were checked at least twice daily by the researchers on the ship.

During the cruise, other meteorological instruments (occasional radiosonde²⁸ and drone meteorological profiling⁵⁹, aerosol concentration monitoring, and samplings) were installed on the ship, which was not used in this study.

Atmospheric reanalysis

This study used an hourly product along the cruise track in ERA5²³. The parameters were cloud-base height, downward shortwave and longwave radiation flux, and ice and liquid water cloud mixing ratio. The closest single grid to the ship was used every hour on the hour. Therefore, the number of samples was much smaller than the observation.

Models

A two-stream, narrow-band radiative transfer model *Streamer* (version 3.0)³⁸ was employed to estimate the radiation profile. The observed surface temperature and profiles of air temperature and relative humidity at 23:30 UTC on 25 December 2022 were used as input for the model (Fig. 3d, e) for thermodynamic structure. For the microphysics, the cloud thickness and liquid (ice) water path were determined by the profile of relative humidity > 95% and 15 g m⁻². The cloud particle size of SLW clouds and ice clouds were set to 20 and 100 μm, respectively.

National Oceanographic and Atmospheric Administration's Hybrid Single-Particle Lagrangian Integrated Trajectory (HYSPLIT) model (version 5.3.2)^{39,56} was also applied to understand the origin of air masses arriving at observation points. Global Forecast System (GFS) data (version 15) on a 0.25° × 0.25° latitude/longitude grid was used as meteorological conditions, including vertical velocity for the HYSPLIT model. Two cases were investigated: one was 25 December 2022, when the SLW clouds were observed at mid-troposphere as shown in Fig. 3, and the other case was 22 February 2023, when ice clouds were observed at mid-troposphere associated with an atmospheric river event²⁸. Three-day 27-ensemble trajectories starting from 3000 m height were obtained for each case.

Data availability

The datasets generated during and/or analyzed during the current study are available on the following website. Microwave radiometer data: <https://ads.nipr.ac.jp/dataset/A20230501-002>, lidar ceilometer data: <https://ads.nipr.ac.jp/dataset/A20230501-003>, surface radiation data: <https://ads.nipr.ac.jp/data/meta/A20230501-006>.

Code availability

The codes to reproduce the analyses presented in this study are available upon request from the corresponding author.

Received: 24 December 2024; Accepted: 19 May 2025

Published online: 28 May 2025

References

- McCoy, D. T., Hartmann, D. L., Zelinka, M. D., Ceppi, P. & Grosvenor, D. P. Mixed-phase cloud physics and Southern Ocean cloud feedback in climate models. *J. Geophys. Res. Atmos.* **120**, 9539–9554 (2015).
- Tan, I., Barahona, D. & Coopman, Q. Potential link between ice nucleation and climate model spread in Arctic amplification. *Geophys. Res. Lett.* **49**, e2021GL097373 (2022).
- Tao, C., Zhang, M. & Xie, S. Cloud radiative effect dominates variabilities of surface energy budget in the dark arctic. *Sci. Rep.* **15**, 2976 (2025).
- Kanji, Z. A. et al. Overview of ice nucleating particles. *Meteorol. Monogr.* **58**, 1.1–13.3 (2017).
- Uetake, J. et al. Airborne bacteria confirm the pristine nature of the Southern Ocean boundary layer. *Proc. Natl. Acad. Sci.* **117**, 13275–13282 (2020).
- Inoue, J., Tobo, Y., Sato, K., Taketani, F. & Maturilli, M. Application of cloud particle sensor sondes for estimating the number concentration of cloud water droplets and liquid water content: case studies in the Arctic region. *Atmos. Meas. Techn.* **14**, 4971–4987 (2021).
- Matsui, H., Kawai, K., Tobo, Y., Iizuka, Y. & Matoba, S. Increasing Arctic dust suppresses the reduction of ice nucleation in the Arctic lower troposphere by warming. *NPJ Clim. Atmos. Sci.* **7**, 266 (2024).
- Korolev, A. V., Isaac, G. A., Cober, S. G., Strapp, J. W. & Hallett, J. Microphysical characterization of mixed-phase clouds. *Q. J. R. Meteorol. Soc.* **129**, 39–65 (2003).
- Schmale, J. et al. Overview of the Antarctic Circumnavigation Expedition: study of preindustrial-like aerosols and their climate effects (ACE-SPACE). *Bull. Am. Meteor. Soc.* **100**, 2260–2283 (2019).
- Trenberth, K. E., Fasullo, J. T., O'Dell, C. & Wong, T. Relationships between tropical sea surface temperature and top-of-atmosphere radiation. *Geophys. Res. Lett.* **37**, 895 (2010).
- McCoy, D. T., Tan, I., Hartmann, D. L., Zelinka, M. D. & Storelvmo, T. On the relationships among cloud cover, mixed-phase partitioning, and planetary albedo in GCMs. *J. Adv. Model. Earth Syst.* **8**, 650–668 (2016).
- Hu, Y. et al. Occurrence, liquid water content, and fraction of supercooled water clouds from combined CALIOP/IIR/MODIS measurements. *J. Geophys. Res. Atmos.* **115**, 569 (2010).
- Zelinka, M. D. et al. Causes of higher climate sensitivity in CMIP6 models. *Geophys. Res. Lett.* **47**, e2019GL085782 (2020).
- Barrett, A. I., Hogan, R. J. & Forbes, R. M. Why are mixed-phase altocumulus clouds poorly predicted by large-scale models? Part 1. Physical processes. *J. Geophys. Res. Atmos.* **122**, 9903–9926 (2017).
- Barrett, A. I., Hogan, R. J. & Forbes, R. M. Why are mixed-phase altocumulus clouds poorly predicted by large-scale models? Part 2. Vertical resolution sensitivity and parameterization. *J. Geophys. Res. Atmos.* **122**, 9927–9944 (2017).

16. Gettelman, A. et al. Simulating observations of Southern Ocean clouds and implications for climate. *J. Geophys. Res. Atmos.* **125**, e2020JD032619 (2020).
17. McCluskey, C. S. et al. Simulating Southern Ocean aerosol and ice nucleating particles in the community earth system model version 2. *J. Geophys. Res. Atmos.* **128**, e2022JD036955 (2023).
18. Dietel, B., Sourdeval, O. & Hoose, C. Characterisation of low-base and mid-base clouds and their thermodynamic phase over the Southern Ocean and Arctic marine regions. *Atmos. Chem. Phys.* **24**, 7359–7383 (2024).
19. Minamihara, Y., Sato, K. & Tsutsumi, M. Kelvin-helmholtz billows in the troposphere and lower stratosphere detected by the pansy radar at syowa station in the antarctic. *J. Geophys. Res. Atmos.* **128**, e2022JD036866 (2023).
20. Kawai, H., Yoshida, K., Koshiro, T. & Yukimoto, S. Importance of minor-looking treatments in global climate models. *J. Adv. Model. Earth Syst.* **14**, e2022MS003128 (2022).
21. Maturilli, M., Herber, A. & König-Langlo, G. Surface radiation climatology for Ny-Ålesund, Svalbard (7.89° N), basic observations for trend detection. *Theor. Appl. Climatol.* **120**, 331–339 (2015).
22. Bodas-Salcedo, A., Andrews, T., Karmalkar, A. V. & Ringer, M. A. Cloud liquid water path and radiative feedbacks over the southern ocean. *Geophys. Res. Lett.* **43**, 10938–10946 (2016).
23. Hersbach, H. et al. The ERA5 global reanalysis. *Q. J. R. Meteorol. Soc.* **146**, 1999–2049 (2020).
24. Mallet, M. D., Alexander, S. P., Protat, A. & Fiddes, S. L. Reducing Southern Ocean shortwave radiation errors in the ERA5 reanalysis with machine learning and 25 years of surface observations. *Artif. Intell. Earth Syst.* **2**, e220044 (2023).
25. Inoue, J. et al. Clouds and radiation processes in regional climate models evaluated using observations over the ice-free Arctic Ocean. *J. Geophys. Res. Atmos.* **126**, e2020JD033904 (2021).
26. Becker, S., Ehrlich, A., Schäfer, M. & Wendisch, M. Airborne observations of the surface cloud radiative effect during different seasons over sea ice and open ocean in the Fram Strait. *Atmos. Chem. Phys.* **23**, 7015–7031 (2023).
27. McFarquhar, G. M. et al. Observations of clouds, aerosols, precipitation, and surface radiation over the southern ocean: An overview of CAPRICORN, MARCUS, MICRE, and SOCRATES. *Bull. Am. Meteor. Soc.* **102**, E894–E928 (2021).
28. Sato, K. & Inoue, J. Ice cloud formation related to oceanic supply of ice-nucleating particles: a case study in the Southern Ocean near an atmospheric river in late summer. *Geophys. Res. Lett.* **50**, e2023GL106036 (2023).
29. Kuma, P. et al. Evaluation of Southern Ocean cloud in the HadGEM3 general circulation model and MERRA-2 reanalysis using ship-based observations. *Atmos. Chem. Phys.* **20**, 6607–6630 (2020).
30. Sato, K., Inoue, J., Kodama, Y.-M. & Overland, J. E. Impact of Arctic sea-ice retreat on the recent change in cloud-base height during autumn. *Geophys. Res. Lett.* **39**, 563 (2012).
31. Wang, Z., Fraser, A. D., Reid, P., O'Farrell, S. & Coleman, R. Antarctic sea ice surface temperature bias in atmospheric reanalyses induced by the combined effects of sea ice and clouds. *Commun. Earth Env.* **5**, 562 (2024).
32. Feofilov, A. G., Stubenrauch, C. J. & Delanoë, J. Ice water content vertical profiles of high-level clouds: classification and impact on radiative fluxes. *Atmos. Chem. Phys.* **15**, 12327–12344 (2015).
33. Stephens, G. L. Radiation profiles in extended water clouds II: parameterization schemes. *J. Atmos. Sci.* **35**, 2123–2132 (1978).
34. Schmidt, J. M., Flatau, P. J. & Yates, R. D. Convective cells in altocumulus observed with a high-resolution radar. *J. Atmos. Sci.* **71**, 2130–2154 (2014).
35. Barrett, P. A., Blyth, A., Brown, P. R. A. & Abel, S. J. The structure of turbulence and mixed-phase cloud microphysics in a highly supercooled altocumulus cloud. *Atmos. Chem. Phys.* **20**, 1921–1939 (2020).
36. Alexander, S. P. et al. Mixed-phase clouds and precipitation in Southern Ocean cyclones and cloud systems observed poleward of 64°S by ship-based cloud radar and lidar. *J. Geophys. Res. Atmos.* **126**, e2020JD033626 (2021).
37. McCann, D. W. Gravity waves, unbalanced flow, and aircraft clear air turbulence. *Nat. Weather Dig.* **25**, 3–14 (2001).
38. Key, J. R. & Schweiger, A. J. Tools for atmospheric radiative transfer: streamer and FluxNet. *Comput. Geosci.* **24**, 443–451 (1998).
39. Rolph, G., Stein, A. & Stunder, B. Real-time environmental applications and display system: ready. *Environ. Model. Softw.* **95**, 210–228 (2017).
40. Rauber, R. M. & Tokay, A. An explanation for the existence of supercooled water at the top of cold clouds. *J. Atmos. Sci.* **48**, 1005–1023 (1991).
41. Hofer, S. et al. Realistic representation of mixed-phase clouds increases future climate warming. *Commun. Earth Env.* **5**, 390 (2023).
42. Cesana, G. V., Khadir, T., Chepfer, H. & Chiriacco, M. Southern Ocean solar reflection biases in CMIP6 models linked to cloud phase and vertical structure representations. *Geophys. Res. Lett.* **49**, e2022GL099777 (2022).
43. Lasher-Trapp, S. et al. Observations and modeling of rime splintering in southern ocean cumuli. *J. Geophys. Res. Atmos.* **126**, e2021JD035479 (2021).
44. McCluskey, C. S. et al. Observations of ice nucleating particles over Southern Ocean waters. *Geophys. Res. Lett.* **45**, 11989–11997 (2018).
45. Vignon, E. et al. Challenging and improving the simulation of mid-level mixed-phase clouds over the high-latitude southern ocean. *J. Geophys. Res. Atmos.* **126**, e2020JD033490 (2021).
46. Moore, K. A. et al. Characterizing ice nucleating particles over the Southern Ocean using simultaneous aircraft and ship observations. *J. Geophys. Res. Atmos.* **129**, e2023JD039543 (2024).
47. Tobo, Y. et al. Glacially sourced dust as a potentially significant source of ice nucleating particles. *Nat. Geosci.* **12**, 253–258 (2019).
48. Kawai, K., Matsui, H. & Tobo, Y. Dominant role of arctic dust with high ice nucleating ability in the arctic lower troposphere. *Geophys. Res. Lett.* **50**, e2022GL102470 (2023).
49. Inoue, J., Tobo, Y., Taketani, F. & Sato, K. Oceanic supply of ice-nucleating particles and its effect on ice cloud formation: a case study in the arctic ocean during a cold-air outbreak in early winter. *Geophys. Res. Lett.* **48**, e2021GL094646 (2021).
50. Forbes, R. M. & Ahlgrim, M. On the representation of high-latitude boundary layer mixed-phase cloud in the ecmwf global model. *Mon. Weather Rev.* **142**, 3425–3445 (2014).
51. Meyers, M. P., DeMott, P. J. & Cotton, W. R. New primary ice-nucleation parameterizations in an explicit cloud model. *J. Appl. Meteorol. Climatol.* **31**, 708–721 (1992).
52. Prenni, A. J. et al. Can ice-nucleating aerosols affect Arctic seasonal climate?. *Bull. Am. Meteor. Soc.* **88**, 541–550 (2007).
53. Tan, I., Oreopoulos, L. & Cho, N. The role of thermodynamic phase shifts in cloud optical depth variations with temperature. *Geophys. Res. Lett.* **46**, 4502–4511 (2019).
54. D'Alessandro, J. J. et al. Characterizing the occurrence and spatial heterogeneity of liquid, ice, and mixed phase low-level clouds over the Southern Ocean using in situ observations acquired during SOCRATES. *J. Geophys. Res.: Atmos.* **126**, e2020JD034482 (2021).
55. Mace, G. G. & Protat, A. Clouds over the Southern Ocean as observed from the R/V Investigator during CAPRICORN. Part I: cloud occurrence and phase partitioning. *J. Appl. Meteorol. Climatol.* **57**, 1783–1803 (2018).
56. Stein, A. F. et al. NOAA's HYSPLIT atmospheric transport and dispersion modeling system. *Bull. Am. Meteor. Soc.* **96**, 2059–2077 (2015).
57. Inoue, J. & Sato, K. Comparison of the depolarization measurement capability of a lidar ceilometer with cloud particle sensor sondes: a case study of liquid water clouds. *Polar Sci.* **35**, 100911 (2023).
58. Vaisala. User Guide Vaisala Lidar Ceilometer CL61. <https://docs.vaisala.com/r/M212475EN-E/en-US> (2022).
59. Inoue, J. & Sato, K. Challenges in detecting clouds in polar regions using a drone with onboard low-cost particle counter. *Atmos. Environ.* **314**, 120085 (2023).
60. Karstens, U., Simmer, C. & Ruprecht, E. Remote sensing of cloud liquid water. *Meteorol. Atmos. Phys.* **54**, 157–171 (1994).

Acknowledgements

This study was supported by the Science Program of the Japanese Antarctic Research Expedition (JARE) as Prioritized Research Projects (AJ1005 and AJ1003), JSPS KAKENHI (grant numbers: JP23H00523 and JP24H02341), and the National Institute of Polar Research (NIPR) through research projects KP-402 and KC-401. The crew of the RV *Shirase* ensured the safety of the JARE64 cruise. Masanori Murakami coordinated all observations on-board the ship. Yasushi Uji and Yusaku Tsurumi supported the installation of the microwave radiometer on the ship. The Japan Meteorological Agency provided radiosonde data at Syowa Station. Dr. Zelinka kindly provided the results of the CMIP cloud fraction data. The authors gratefully acknowledge the NOAA Air Resources Laboratory (ARL) for the provision of the HYSPLIT transport and dispersion model and/or READY website (<https://www.ready.noaa.gov>) used in this publication. We thank Martha Evonuk, PhD, from Edanz (<https://jp.edanz.com/ac>), for editing this manuscript and helping to draft the abstract. The constructive comments from referees were greatly helpful in improving the manuscript.

Author contributions

Jl and KS planned and conducted the observations and performed the analysis. SS provided a microwave radiometer and its data. Jl wrote the manuscript with inputs from all co-authors.

Competing interests

The authors do not have any conflict of interest/Competing interests.

Additional information

Supplementary Information The online version contains supplementary material available at <https://doi.org/10.1038/s41598-025-03119-z>.

Correspondence and requests for materials should be addressed to J.I.

Reprints and permissions information is available at www.nature.com/reprints.

Publisher's note Springer Nature remains neutral with regard to jurisdictional claims in published maps and institutional affiliations.

Open Access This article is licensed under a Creative Commons Attribution-NonCommercial-NoDerivatives 4.0 International License, which permits any non-commercial use, sharing, distribution and reproduction in any medium or format, as long as you give appropriate credit to the original author(s) and the source, provide a link to the Creative Commons licence, and indicate if you modified the licensed material. You do not have permission under this licence to share adapted material derived from this article or parts of it. The images or other third party material in this article are included in the article's Creative Commons licence, unless indicated otherwise in a credit line to the material. If material is not included in the article's Creative Commons licence and your intended use is not permitted by statutory regulation or exceeds the permitted use, you will need to obtain permission directly from the copyright holder. To view a copy of this licence, visit <http://creativecommons.org/licenses/by-nc-nd/4.0/>.

© The Author(s) 2025